Plasmon-Enhanced Photocatalytic Activity of Iron Oxide on Gold Nanopillars

Hanwei Gao,[†,§] Chong Liu,[†,§] Hoon Eui Jeong,[†] and Peidong Yang[†,‡,*]

[†]Department of Chemistry, University of California, Berkeley, California 94720, United States and [‡]CEAMR-KAU, King Abudulaziz University, Jeddah 21589, Saudi Arabia. [§]These authors contributed equally to this work.

Photocatalytic water splitting is a promising approach to produce fuel using solar energy.[1−8] While semiconductors in photovoltaic devices generate electricity, semiconductors in water splitting use photogenerated charge carriers to facilitate the evolution of oxygen and hydrogen.[2,5] Increasing the number of charge carriers that can reach the semiconductor−electrolyte interface is essential to a higher light-harvesting efficiency; however, the length over which the charge collection takes place is typically shorter than the depth at which photons are absorbed.[5,9] Here, we demonstrate an enhanced photocurrent of iron oxide (hematite) photoanodes by coating the semiconductor thin film on Au nanopillars. The enhancement can be attributed to increased optical absorption originating from both surface plasmon resonances and photonic-mode light trapping within the nanostructured topography. The resonances can be tuned to desirable wavelengths by varying the thickness of the iron oxide layer. A net enhancement as high as 50% was observed over the solar spectrum. Our results provide a general, widely applicable solution to concentrating light in the active regions of semiconductors. Such optical engineering methods are fully compatible with and independent of efforts on material quality optimization, which together can lead to improved performance of solar-driven water splitting.

Much work so far has focused on wide band gap semiconductors for water splitting for the sake of chemical stability. For optimal optical absorption, however, it is desirable to use materials with smaller band gaps (*e.g.*, $E_g < 2.5$ eV) so that the significant part of solar radiation in the visible range can be utilized.[10] Hematite Fe_2O_3 has been identified as an excellent candidate for photoanodes in water splitting because it is

ABSTRACT
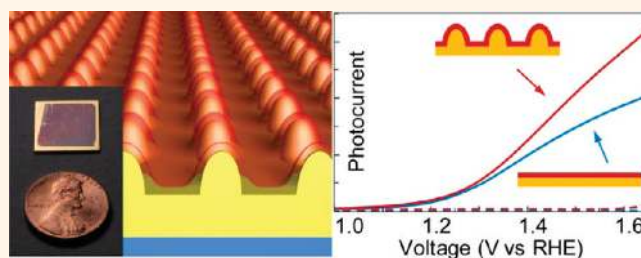
Photocatalytic water splitting represents a promising way to produce renewable hydrogen fuel from solar energy. Ultrathin semiconductor electrodes for water splitting are of particular interest because the optical absorption occurs in the region where photogenerated charge carriers can effectively contribute to the chemical reactions on the surface. It is therefore important to manipulate and concentrate the incident light so that more photons can be absorbed within the thin film. Here we show an enhanced photocurrent in a thin-film iron oxide photoanode coated on arrays of Au nanopillars. The enhancement can be attributed primarily to the increased optical absorption originating from both surface plasmon resonances and photonic-mode light trapping in the nanostructured topography. The resonances can be tuned to a desirable wavelength by varying the thickness of the iron oxide layer. A net enhancement as high as 50% was observed over the solar spectrum.

KEYWORDS: plasmonic · iron oxide · photoanode · photocurrent · nanograting

earth-abundant, cost-effective, photoelectrochemically stable, and, most importantly, has a desirable band gap of 2.2 eV.[11−19] Unfortunately, severe bulk recombination was reported in Fe_2O_3 so that the charge carriers generated in only a very thin layer (a few nanometers without bias[20] and tens of nanometers with bias[21,22]) near the interface with the electrolyte can contribute effectively to the reactions on the surface of the Fe_2O_3 electrode. Plasmonic and photonic nanostructures have shown promise in manipulating and concentrating light in photocatalytic and photovoltaic devices, which can lead to enhanced photon absorption in the thin, effective layer of the semiconductor.[23−28]

In this work, we use arrays of Au nanopillars as both electrical contacts and plasmonic couplers to achieve enhanced photoactivity of Fe_2O_3 photoanodes. Compared to metal nanoparticles that exhibit extremely confined localized plasmon resonances,[27,29,30] the nanostructured continuous Au substrates sustain surface plasmon modes whose evanescent fields exhibit much longer decay lengths.[31] Therefore, pronounced enhancement can be achieved with the Au nanopillars buried under the Fe_2O_3 layer, avoiding issues such as interference of the metal in the chemical reaction processes and loss of incoming light absorbed by metal particles placed near the semiconductor—electrolyte interface.[32]

RESULTS AND DISCUSSION

Fe_2O_3 electrodes on large-area arrays of Au nanopillars were fabricated on the basis of nanoimprinting techniques[33] (Figure 1a and Methods). To generate surface plasmon modes in visible wavelengths at the Au–Fe_2O_3 interface, we patterned the nanopillars in periodic lattices with 700 nm pitch. A layer of 200 nm Au was first evaporated onto quartz substrates followed by spin-coating nominally 500 nm thick poly(methyl methacrylate) (PMMA). Square arrays of cylindrical holes were generated in the PMMA layer, inversely replicating the nanorod array (on 700 nm pitches) structures in the polyurethane nanoimprinting molds. Using a layer of electron-beam-evaporated Cr as an etching mask, the cylindrical holes were further deepened by plasma etching. Au nanopillars were then obtained after directional electron beam evaporation of Au followed by PMMA liftoff. The Au nanopillars were 300 nm in height and had a base diameter of about 300 nm, approximately equal to the diameter of the nanorods in the polyurethane molds. The top of the nanopillars had a smaller diameter because of the apertures in the Cr mask shrank as Au was evaporated on it. The arrays of Au nanopillars were highly uniform on a centimeter scale (Figure 1b inset) and can be potentially further scaled up owing to the scalability of nanoimprinting techniques. The photoanodes were completed with a 90 nm thin-film coating of Fe_2O_3. Metallic Fe was evaporated onto the patterned Au substrates and annealed in pure oxygen at 450 °C for about one hour. Conformal coating of the Fe_2O_3 layer can be seen in the tilt-angle scanning electron microscopy (SEM) image (Figure 1c). The annealed Fe_2O_3 layer resembles the cauliflower-like morphology reported previously[34] (Figure 1d). X-ray diffraction indicated complete conversion from Fe to hematite Fe_2O_3 (Figure S1).

A net enhancement of photocurrent under AM1.5 simulated solar illumination was observed from the Fe_2O_3 nanopillar photoanodes as compared to a planar control sample (Figure 2). The measurement was
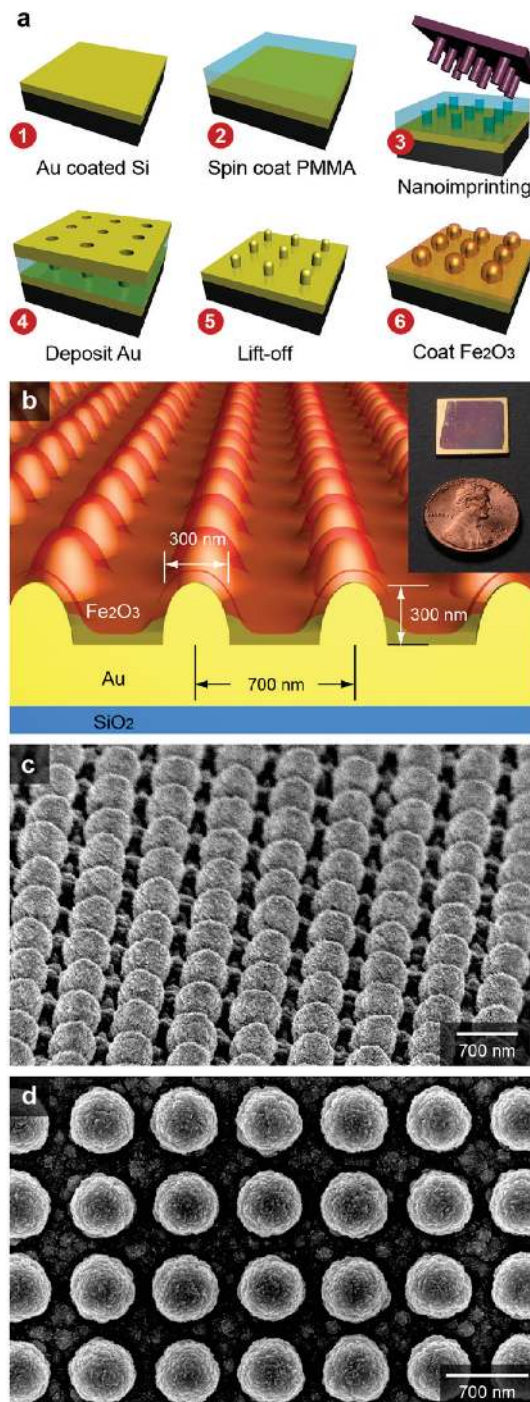

Figure 1. Fe_2O_3 photoanode on arrays of Au nanopillars. (a) Steps of the fabrication procedure. **(b)** The geometry of the Au nanopillars is shown schematically. The nanopillars are 300 nm in diameter at the base and 300 nm in height. Connected by a 200 nm thick planar Au film, the nanopillars were patterned in square arrays with 700 nm pitch. Inset: photograph of a 1.5 × 1.5 cm^2 sample uniformly patterned with Au nanopillars with a penny for perspective. **(c)** 30° tilted and **(d)** top view scanning electron microscopy (SEM) images of 90 nm of Fe_2O_3 coated on a Au nanopillar array.

carried out in 1 M NaOH electrolyte using a three-electrode configuration with Ag/AgCl reference electrode and platinum mesh counter electrode. The Fe_2O_3 electrode was illuminated by 100 mW/cm^2 light from a
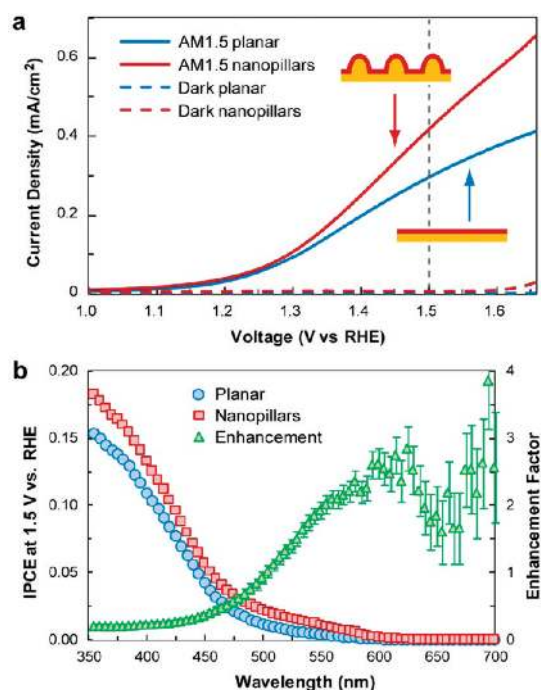
a

b

Figure 2. Enhanced photocurrent from 90 nm Fe_2O_3 coated on an Au nanopillar array. (a) The $I-V$ curves show enhancement of the photocurrent from the patterned Fe_2O_3 electrode as compared to the planar control under AM1.5 simulated solar illumination. (b) The IPCE spectra (circles and squares) were obtained using spectrally resolved photocurrent measurements. Distinct enhancement can be observed as peaks (triangles) in visible wavelengths.

300 W xenon arc lamp through an AM1.5 solar simulation filter. The measured photocurrent was normalized to the sample's macroscopic area to obtain the photocurrent density (in units of mA/cm^2) for comparison. A photocurrent enhancement higher than 40% was achieved at 1.5 V vs RHE (reversible hydrogen electrode) (Figure 2a). The dark current remained low even beyond 1.6 V vs RHE, which indicated high-quality conformal coating of the Fe_2O_3 on the Au nanopillars. Interestingly, the onset voltage of the photocurrent remained nearly the same for both the planar and the patterned photoanodes. In photoelectrochemical reactions, the total quantum efficiency is limited by recombination of photogenerated charge carriers both in the semiconductor's bulk and at the semiconductor−electrolyte interface. Under low bias, surface recombination, which originates from surface states and interface barriers, is the dominant effect in the oxygen evolution reaction on Fe_2O_3 photoanodes. Such surface barriers become less effective under higher bias, where the bulk recombination then becomes the limiting factor and the photocurrent approaches a plateau.[35] The fact that constant onset voltage was observed regardless of nanopatterning of the surface indicates that the nanopillar structures had minimal influence on the chemical processes occurring at the semiconductor−electrolyte interface. Therefore, the significant enhancement of photocurrent under high
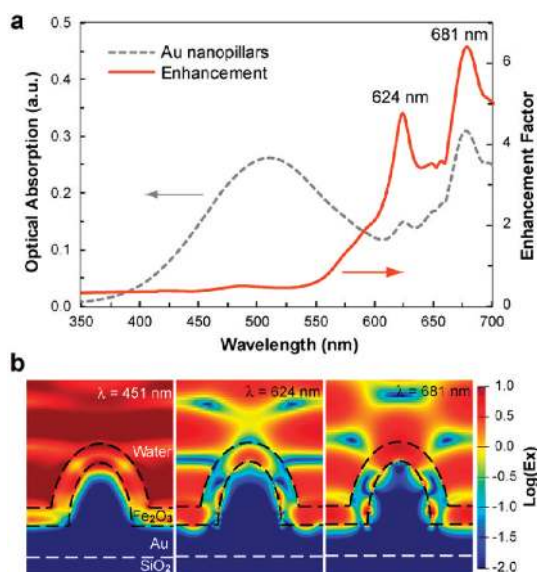

a

b

Figure 3. Enhanced optical absorption simulated using finite difference time domain methods. (a) Well-defined peaks are observed in the simulated absorption enhancement spectrum of Fe_2O_3 at 624 and 681 nm (solid curve), which agree well with the measured enhancement in IPCE. Peaks at the same wavelengths are also found in the simulated absorption spectrum of Au nanopillars (dashed curve), indicating that the photocurrent enhancement obtained in nanopatterned Fe_2O_3 electrodes is induced by surface plasmon resonances. (b) Electric field distribution maps from the FDTD simulations verified the plasmonic resonances at 624 and 681 nm with the characteristic evanescent field patterns near the Fe_2O_3−Au interfaces. Moreover, the field map at a nonresonant wavelength (451 nm) indicates that photonic-mode light trapping is responsible for the enhancement in a broader spectral range.

bias was caused mainly by enhanced optical absorption in the Fe_2O_3 thin film that led to an increased number of photogenerated charge carriers.

The incident photon-to-current efficiency (IPCE), obtained via spectrally resolved photocurrent measurements, showed a clear wavelength dependence of the photocurrent enhancement (Figure 2b). Well-defined peaks in the enhancement in visible wavelengths were observed with magnitudes higher than 2.5. While the enhancement spectrum reaches these maxima at long wavelengths, the peaks are so broad that significant enhancement occurs starting from 500 nm around the band gap of Fe_2O_3. In contrast, the photocurrent enhancement was much lower at wavelengths shorter than 500 nm, where the intrinsic interband transitions in Au suppress the surface plasmon resonances.[36] Although the higher photocurrent enhancement is located in the spectral region where the incident photon to current efficiency is low, a large portion of the power in solar radiation comes from light in the visible region, which accounts for the considerable net enhancement of photocurrent under solar-simulated illumination.

These spectral features of the IPCE enhancement can be attributed to the electric field of the plasmonic resonances that originates from the modulated

Fe_2O_3—Au interface and results in enhanced optical absorption. The mechanisms were verified by numerical electromagnetic simulations (Figure 3). Optical absorption spectra of the Fe_2O_3 layer on patterned and planar Au substrates were calculated using three-dimensional full-field finite difference time domain methods (Lumerical FDTD Solution 7.5). A large increase in the absorption was observed with peaks at 624 and 681 nm (Figure 3a), which matches well with the experimentally measured IPCE enhancement spectrum. When surface plasmon resonances are generated, the collective charge oscillations at the metal surface cause increased ohmic loss of electromagnetic energy, which can be visualized as peaks in the spectrally resolved absorption in the metal.[37] While the absorption in the semiconductor and in the metallic sections is hard to distinguish experimentally, theoretical simulations provide a powerful tool to gain microscopic insights. By integrating the absorption only in the Au regions, the electromagnetic energy dissipated in the Au was obtained theoretically (Figure 3a). The two plasmonic resonances at longer wavelengths (>600 nm) in the absorption spectrum of the Au nanopillars coincide with the peak wavelengths of the enhancement of absorption in Fe_2O_3, which verifies that generation of the surface plasmons within the Au nanopillar arrays is responsible for the calculated absorption enhancement and the measured photocurrent enhancement. It is worth noting that the peaks in the measured enhancement spectrum are much broader than the calculated plasmonic resonances. Such a discrepancy is often observed between experiments and simulations and can be attributed to a variety of factors such as the variation of the unit cell geometry, the surface roughness that is inevitable in reality but not considered in theory, and imperfect collimation of the optical illumination. This broadening effect appears to be quite important to the enhanced photocurrent achieved here. Much of the enhancement arises in the spectral range from 500 to 600 nm, where the shoulder of the plasmon resonance and a considerable absorption coefficient in the Fe_2O_3 coexist.

The IPCE spectra can also be used to deconvolute the enhancement from plasmonic fields and other effects such as microscopic surface area of the photoelectrode. The solid—electrolyte interface area is particularly important for electrochemical processes. One may be concerned that the enhanced photocurrent observed here is merely originated from the increased surface area of the nanostructured electrode. In fact, the contribution from surface area increase is indicated by the IPCE spectrum below 400 nm, where surface plasmons are known to be suppressed in Au. It is found that about 15% enhancement of IPCE around 400 nm (Figure 2a) is much smaller than the 30% increase of the surface area for an electrode with nanopillars. It is worth noting that this 15% is inevitably an
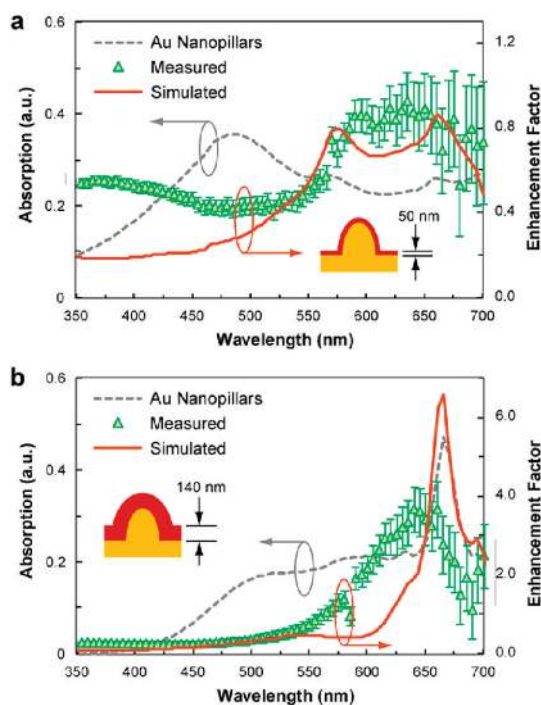

Figure 4. Tunable enhancement by varying the thickness of Fe_2O_3. Photoanodes of Fe_2O_3 on Au nanopillars with different thicknesses were investigated. The surface plasmon resonances, shifted to (a) shorter wavelengths with 50 nm Fe_2O_3 and (b) longer wavelengths with 140 nm Fe_2O_3, are shown in the simulated absorption in Au nanopillars (dashed curves) and absorption enhancement in Fe_2O_3 (solid curves). The shifted peaks are also observed in the measured IPCE spectra (triangles).

overestimation of the influence from surface area increase because other nonplasmonic effects such as photonic scattering can still take effect in this spectral region. Therefore, the enhancement of photocurrent resulting from the surface area increase is quite modest compared to the distinct plasmonic resonance in the spectra.

As further evidence for the plasmonic nature of the measured enhancement, the plasmonic characteristics at both enhancement peaks (624 and 681 nm) can be observed in the electric field distribution maps provided by the FDTD simulations (Figure 3b). The plasmonic evanescent waves featured with spatially confined and highly intense electromagnetic fields show maximum amplitudes around the nanopillars at the Fe_2O_3—Au interface, which decay exponentially into the bulk of Fe_2O_3. The effective optical absorption of the Fe_2O_3 that contributes to photocurrent decreases as the distance to the Fe_2O_3—electrolyte interface increases. Because of the bulk recombination, only the photogenerated charge carriers within a thin layer of the active material close to the semiconductor—electrolyte interface can reach the aqueous solution and contribute to the electrochemical reaction. Therefore, the photocurrent enhancement measured on 90 nm thick Fe_2O_3 is smaller than the calculated absorption enhancement around the plasmonic resonances.

In addition to the evanescent field patterns around the nanopillars, photonic-mode light trapping is another important factor for the enhanced photocurrent in Fe_2O_3 coated on Au nanopillars. This light-trapping effect can be identified by the intense electric field in the planar region between adjacent nanopillars in the simulated field distribution maps (Figure 3b). In contrast to the plasmonic modes, which have the largest field amplitude at the Fe_2O_3—Au interface, the electric field of the photonic-mode light trapping maximizes in the middle of the Fe_2O_3 layer.[38] The photonic-mode light trapping is responsible for the enhanced optical absorption in a much broader spectral region. At wavelengths other than the plasmonic resonances (*e.g.*, 450 nm), photonic-mode trapping can be observed both between and around the nanopillars, while the evanescent field is not present (Figure 3b). Compared to the simplified, extremely smooth surfaces in theoretical simulations, the samples in the experiments benefit from substantial surface roughness, which resulted in more significant photonic-mode light trapping, an effect that has been used in solar cells with intentionally roughened back electrodes.[39] Therefore, the measured photocurrent enhancement is generally higher than the calculated absorption enhancement at wavelengths far from the plasmon resonances.

The wavelengths of enhanced photocurrent can be tuned by changing the thickness of the Fe_2O_3. Surface plasmon resonances depend upon the electric permittivity of the environment surrounding the metallic nanostructures.[31] Because of the subwavelength thickness of the Fe_2O_3 layer in our experiments, the plasmon resonances of the metal experience an effective refractive index that is the average of the refractive index of the Fe_2O_3 layer and the aqueous solution.[40−42] By reducing the Fe_2O_3 thickness to 50 nm, the effective refractive index was reduced (Fe_2O_3 has a higher refractive index than water) and the plasmon resonances shifted to shorter wavelengths (Figure 4a). Consistently, the spectrum of the photocurrent enhancement also shows blue-shifted peaks (Figure 4a). Although the surface plasmon resonances in the case of the 50 nm thick Fe_2O_3 exhibited a smaller amplitude in the simulated absorption spectrum of Au nanopillars, the blue-shifted resonances led to higher enhancement at wavelengths with higher IPCE in Fe_2O_3, which yielded a net photocurrent enhancement of about 50% at 1.5 V *vs* RHE (Figure S2). We also demonstrated that by increasing the thickness of the Fe_2O_3, the peak of the photocurrent enhancement shifted to a longer wavelength, which agreed well with the red-shifted plasmonic resonances predicted by the FDTD simulation (Figure 4b).

The intrinsic absorption coefficient of semiconductor materials, the photoactivity of electrodes, the resonances of surface plasmons, and the power density of solar radiation are all wavelength dependent. It is, therefore, critical to match the spectral profiles of these properties for optimized photocurrent enhancement by improving effective photon absorption. The significant photocurrent enhancement observed here takes advantage of both the surface plasmon resonances in the visible range sustained by the Au nanopillars and the relatively low band gap of the active semiconductor Fe_2O_3. The effects demonstrated here, however, should not be limited to the Fe_2O_3—Au combination. Plasmonic metals such as Ag, Al, and Pd sustain resonances in the UV region[43] and can be selected to pair with photoactive materials with wider band gaps including WO_3[44] and TiO_2.[1] Recent advances in alloyed plasmonic metals can be particularly interesting because they are more chemically stable while retaining pronounced plasmonic resonances.[45,46] Furthermore, the thickness of the thin semiconductor layer provides an extra dimension to tune the plasmon resonances. Together with the nanoimprinting-based fabrication processes, the metallic nanopillar arrays offer a controllable and scalable platform to tailor plasmonic and photonic resonances for efficient solar water splitting.

METHODS

Preparation of Nanostructured Photoanodes. Au (200 nm), with a thin Ti adhesion layer, was deposited onto quartz substrates using electron beam evaporation. A layer of nominally 500 nm PMMA thin film was spin-coated onto Au and imprinted against a polyurethane mold at about 130 °C for 20 min. The polyurethane mold was replicated from a silicon master (homemade using photolithography), which contained square arrays of 300 nm diameter cylindrical rods with 700 nm pitch. The imprinted PMMA has the inverted nanostructures (*i.e.*, cylindrical holes). Chromium (5 nm) was then evaporated from a glancing angle (*ca.* 80°) onto the patterned PMMA as an etching mask. The holes in the PMMA thin film were deepened using plasma etching (50 W for 5 min in 90 mTorr Oxygen, Plasma-Therm PK-12) until the Au surface was exposed. After directional Au deposition using electron beam evaporation at a slow rate (1 A/s) followed by PMMA liftoff in acetone, arrays of Au nanopillars were obtained on continuous Au substrates. The photoanode material Fe_2O_3 was coated on the Au surface using electron-beam-evaporated metallic Fe followed by annealing in pure oxygen at 450 °C for about one hour.

Photoelectrochemical Measurements. The photocurrent was measured in a three-electrode photoelectrochemical cell with Ag/AgCl as the reference electrode and meshed platinum as the counter electrode. A 1 M NaOH solution was used as the electrolyte. The illumination was from a 300 W xenon arc lamp (Newport 66984) through an AM1.5 solar simulation filter (Newport 2 × 2 in^2 AM 1.5 Global). The power density of the illumination was calibrated to be 100 mW/cm^2 using a standardized photodiode (Hamamatsu). The I—V curves were obtained using a potentiostat (Gamry Reference 600) with a scan rate of 10 mV/s. To obtain the photocurrent density, the measured photocurrent was normalized to the macroscopic area of the sample. Although microscopic surface areas are sometimes

considered for nanostructures, in this work the effective optical absorption determines the overall activity of the photoelectrode. Therefore, photocurrent density calculated using macroscopic area shows the ability of photon-to-electron conversion of the electrode. For IPCE measurements, light from the xenon lamp was dispersed by a monochromator (Newport Corp.), and the photocurrent was recorded at a constant bias (1.5 V *vs* RHE) with a spectral step of 5 nm (bandwidth of the light delivered from the monochromator is about 15 nm). The measured photocurrent was converted to IPCE by normalizing to a standard photodiode with a known quantum efficiency. The enhancement factor was calculated by $(\eta_{nanopillar} - \eta_{planar})/\eta_{planar}$.

Numerical Electromagnetic Simulations. The optical properties of Fe_2O_3 on Au nanopillars were simulated using three-dimensional full-field finite difference time domain methods (Lumerical FDTD Solutions 7.5). Broadband linearly polarized plane waves were perpendicularly incident onto individual nanopillars with periodic in-plane boundary conditions. Meshing size as small as 3 nm was used in the regions containing Fe_2O_3 and Au materials, which was proven fine enough in convergence tests. The field vectors were monitored in three-dimensional grid points to extract absorption spectra of Fe_2O_3 and Au, respectively, and to generate field distribution maps at wavelengths of interest.

Supporting Information Available: (1) XRD of Fe_2O_3 thin film on planar Au. (2) Photocurrent from Fe_2O_3 with different thicknesses. This material is available free of charge via the Internet at http://pubs.acs.org.

REFERENCES AND NOTES

1. Fujishima, A.; Honda, K. Electrochemical Photolysis of Water at a Semiconductor Electrode. *Nature* **1972**, *237*, 37–38.
2. Grätzel, M. Photoelectrochemical Cells. *Nature* **2001**, *414*, 338–344.
3. Zou, Z.; Ye, J.; Sayama, K.; Arakawa, H. Direct Splitting of Water under Visible Light Irradiation with an Oxide Semiconductor Photocatalyst. *Nature* **2001**, *414*, 625–627.
4. Chen, Z.; Jaramillo, T. F.; Deutsch, T. G.; Kleiman-Shwarsctein, A.; Forman, A. J.; Gaillard, N.; Garland, R.; Takanabe, K.; Heske, C.; Sunkara, M.; *et al*. Accelerating Materials Development for Photoelectrochemical (PEC) Hydrogen Production: Standards for Methods, Definitions, and Reporting Protocols. *J. Mater. Res.* **2010**, *25*, 3–16.
5. Walter, M.; Warren, E.; McKone, J.; Boettcher, S. W.; Qixi, M.; Santori, L.; Lewis, N. S. Solar Water Splitting Cells. *Chem. Rev.* **2010**, *110*, 6446–6473.
6. Maeda, K.; Teramura, K.; Lu, D.; Takata, T.; Saito, N.; Inoue, Y.; Domen, K. Photocatalyst Releasing Hydrogen from Water. *Nature* **2006**, *440*, 295.
7. Hwang, Y. J.; Boukai, A.; Yang, P. Highly Aligned N-Si/N-TiO₂ Core/Shell Nanowire Arrays with Enhanced Photoactivity. *Nano Lett.* **2009**, *9*, 410–415.
8. Hou, Y.; Abrams, B. L.; Vesborg, P. C. K.; Björketun, M. E.; Herbst, K.; Bech, L.; Setti, A. M.; Damsgaard, C. D.; Pedersen, T.; Hansen, O.; *et al*. Bioinspired Molecular Co-Catalysts Bonded to a Silicon Photocathode for Solar Hydrogen Evolution. *Nat. Mater.* **2011**, *10*, 434–438.
9. Cesar, I.; Sivula, K.; Kay, A.; Zboril, R.; Grätzel, M. Influence of Feature Size, Film Thickness, and Silicon Doping on the Performance of Nanostructured Hematite Photanodes for Solar Water Splitting. *J. Phys. Chem. C* **2009**, *113*, 772–782.
10. Bolton, J. R.; Strickler, S. J.; Connolly, J. S. Limiting and Realizable Efficiencies of Solar Photolysis of Water. *Nature* **1985**, *316*, 495–500.
11. Dare-Edwards, M. P.; Goodenough, J. B.; Hamnett, A.; Trevellick, P. R. Electrochemistry and Photoelectrochemistry of Iron(III) Oxide. *J. Chem. Soc., Faraday Trans. 1* **1983**, *79*, 2027–2041.
12. Kay, A.; Cesar, I.; Grätzel, M. New Benchmark for Water Photooxidation by Nanostructured A-Fe₂O₃ Films. *J. Am. Chem. Soc.* **2006**, *128*, 15714–15721.
13. Lin, Y.; Zhou, S.; Sheehan, S. W.; Wang, D. Nanonet-Based Hematite Heteronanostructures for Efficient Solar Water Splitting. *J. Am. Chem. Soc.* **2011**, *133*, 2398–2401.
14. Formal, F. L.; Grätzel, M.; Sivula, K. Controlling Photoactivity in Ultrathin Hematite Films for Solar Water-Splitting. *Adv. Funct. Mater.* **2010**, *20*, 1099–1107.
15. Ling, Y.; Wang, G.; Wheeler, D. A.; Zhang, J. Z.; Li, Y. Sn-Doped Hematite Nanostructures for Photoelectrochemical Water Splitting. *Nano Lett.* **2011**, *11*, 2119–2125.
16. Kennedy, J. H.; Karl W. Frese, J. Flatband Potentials and Donor Densities of Polycrystalline Alpha-Fe₂O₃ Determined from Mott-Schottky Plots. *J. Electrochem. Soc.* **1978**, *125*, 723–726.
17. Kennedy, J. H.; Anderman, M.; Shinar, R. Photoactivity of Polycrystalline Alpha-Fe₂O₃ Electrodes Doped with Group IVa Elements. *J. Electrochem. Soc.* **1981**, *128*, 2371–2373.
18. Sivula, K.; Formal, F. L.; Grätzel, M. Solar Water Splitting: Progress Using Hematite (A-Fe₂O₃) Photoelectrodes. *ChemSusChem* **2011**, *4*, 432–449.
19. Lin, Y.; Yuan, G.; Sheehan, S.; Zhou, S.; Wang, D. Hematite-Based Solar Water Splitting: Challenges and Opportunities. *Energy Environ. Sci.* **2011**Advanced Article.
20. Kennedy, J. H.; Anderman, M.; Shinar, R. Photoactivity of Polycrystalline Alpha-Fe₂O₃ Electrodes Doped with Group IVa Elements. *J. Electrochem. Soc.* **1981**, *11*, 2371–2373.
21. Morrison, S. R. *Electrochemistry at Semiconductor and Oxidized Metal Electrodes*, 1st ed.; Springer: Berlin, 1980.
22. Tomkiewicz, M.; Fay, H. Photoelectrolysis of Water with Semiconductors. *Appl. Phys.* **1979**, *18*, 1.
23. Zhu, J.; Hsu, C.-M.; Yu, Z.; Fan, S.; Cui, Y. Nanodome Solar Cells with Efficient Light Management and Self-Cleaning. *Nano Lett.* **2010**, *10*, 1979–1984.
24. Kelzenberg, M. D.; Boettcher, S. W.; Petykiewicz, J. A.; Turner-Evans, D. B.; Putnam, M. C.; Warren, E. L.; Spurgeon, J. M.; Briggs, R. M.; Lewis, N. S.; Atwater, H. A. Enhanced Absorption and Carrier Collection in Si Wire Arrays for Photovoltaic Applications. *Nat. Mater.* **2010**, *9*, 239–244.
25. Boettcher, S. W.; Spurgeon, J. M.; Putnam, M. C.; Warren, E. L.; Turner-Evans, D. B.; Kelzenberg, M. D.; Maiolo, J. R.; Atwater, H. A.; Lewis, N. S. Energy-Conversion Properties of Vapor-Liquid-Solid-Grown Silicon Wire-Array Photocathodes. *Science* **2010**, *327*, 185–187.
26. Yu, Z.; Raman, A.; Fan, S. Fundamental Limit of Nanophotonic Light Trapping in Solar Cells. *Proc. Natl. Acad. Sci.* **2010**, *107*, 17491–17496.
27. Thomann, I.; Pinaud, B. A.; Chen, Z.; Clemens, B. M.; Jaramillo, T. F.; Brongersma, M. L. Plasmon Enhanced Solar-to-Fuel Energy Conversion. *Nano Lett.* **2011**, *11*, ASAP.
28. Ding, I.-K.; Zhu, J.; Cai, W.; Moon, S.-J.; Cai, N.; Wang, P.; Zakeeruddin, S. M.; Grätzel, M.; Brongersma, M. L.; Cui, Y.; McGehee, M. D. Plasmonic Dye-Sensitized Solar Cells. *Adv. Energy Mater.* **2011**, *1*, 52–57.
29. Liu, Z.; Hou, W.; Pavaskar, P.; Aykol, M.; Cronin, S. B. Plasmon Resonant Enhancement of Photocatalytic Water Splitting under Visible Illumination. *Nano Lett.* **2011**, *11*, 1111–1116.
30. Chen, J.-J.; Wu, J. C. S.; Wu, P. C.; Tsai, D. P. Plasmonic Photocatalyst for H₂ Evolution in Photocatalytic Water Splitting. *J. Phys. Chem. C* **2011**, *115*, 210–216.
31. Raether, H. *Surface Plasmons on Smooth and Rough Surfaces and on Gratings*; Springer: Berlin, 1988.
32. Thimsen, E.; Formal, F. l.; Graetzel, M.; Warren, S. C. Influence of Plasmonic Au Nanoparticles on the Photoactivity of Fe₂O₃ Electrodes for Water Splitting. *Nano Lett.* **2011**, *11*, 35–43.
33. Choi, S.-J.; Yoo, P. J.; Baek, S. J.; Kim, T. W.; Lee, H. H. An Ultraviolet-Curable Mold for Sub-100-nm Lithography. *J. Am. Chem. Soc.* **2004**, *126*, 7744–7745.
34. Tilley, S. D.; Cornuz, M.; Sivula, K.; Grätzel, M. Light-Induced Water Splitting with Hematite: Improved Nanostructure and Iridium Oxide Catalysis. *Angew. Chem., Int. Ed.* **2010**, *49*, 6405–6408.
35. Dotan, H.; Sivula, K.; Grätzel, M.; Rothschild, A.; Warren, S. C. Probing the Photoelectrochemical Properties of Hematite

(A-Fe$_2$O$_3$) Electrodes Using Hydrogen Peroxide as a Hole Scavenger. *Energy Environ. Sci.* **2011**, *4*, 958–964.

36. Maier, S. A. *Plasmonics: Fundamentals and Applications*, 1st ed.; Springer: Berlin, 2007.

37. Barnes, W. L.; Murray, W. A.; Dintinger, J.; Devaux, E.; Ebbesen, T. W. Surface Plasmon Polaritons and Their Role in the Enhanced Transmission of Light through Periodic Arrays of Subwavelength Holes in a Metal Film. *Phys. Rev. Lett.* **2004**, *92*, 107401.

38. Ferry, V. E.; Sweatlock, L. A.; Pacifici, D.; Atwater, H. A. Plasmonic Nanostructure Design for Efficient Light Coupling into Solar Cells. *Nano Lett.* **2008**, *8*, 4391–4397.

39. Müller, J.; Recha, B.; Springerb, J.; Vanecekb, M. TCO and Light Trapping in Silicon Thin Film Solar Cells. *Solar Energy* **2004**, *77*, 917–930.

40. Malinsky, M. D.; Kelly, K. L.; Schatz, G. C.; Duyne, R. P. V. Chain Length Dependence and Sensing Capabilities of the Localized Surface Plasmon Resonance of Silver Nanoparticles Chemically Modified with Alkanethiol Self-Assembled Monolayers. *J. Am. Chem. Soc.* **2001**, *123*, 1471–1482.

41. Damos, F. S.; Luz, R. C. S.; Kubota, L. T. Determination of Thickness, Dielectric Constant of Thiol Films, and Kinetics of Adsorption Using Surface Plasmon Resonance. *Langmuir* **2005**, *21*, 602–609.

42. Chien, F.-C.; Chen, S.-J. Direct Determination of the Refractive Index and Thickness of a Biolayer Based on Coupled Waveguide-Surface Plasmon Resonance Mode. *Opt. Express* **2006**, *31*, 187–189.

43. Gao, H.; Henzie, J.; Lee, M. H.; Odom, T. W. Screening Plasmonic Materials Using Pyramidal Gratings. *Proc. Natl. Acad. Sci.* **2008**, *105*, 20146–20151.

44. Santato, C.; Odziemkowski, M.; Ulmann, M.; Augustynski, J. Crystallographically Oriented Mesoporous WO$_3$ Films: Synthesis, Characterization, and Applications. *J. Am. Chem. Soc.* **2001**, *123*, 10639–10649.

45. Link, S.; Wang, Z. L.; El-Sayed, M. A. Alloy Formation of Gold-Silver Nanoparticles and the Dependence of the Plasmon Absorption on Their Composition. *J. Phys. Chem. B* **1999**, *103*, 3529–3533.

46. Szunerits, S.; Castel, X.; Boukherroub, R. Surface Plasmon Resonance Investigation of Silver and Gold Films Coated with Thin Indium Tin Oxide (ITO) Layers: Influence on Stability and Sensitivity. *J. Phys. Chem. C* **2008**, *112*, 15813–15817.